

Toward Long-Term Monitoring of Regional Permafrost Thaw with Satellite InSAR

Taha Sadeghi Chorsi, Franz J. Meyer Timothy. H. Dixon

Abstract

~~We estimate active~~ Active layer thickness (ALT) ~~is estimated for part of northern~~ study area in Northern Alaska's continuous permafrost zone ~~for summer 2017 to 2022~~ using satellite data from Sentinel-1 (radar) and ICESat-2. ~~Interferograms (LiDAR) for the period 2017 to 2022. Synthetic Aperture Radar (SAR) interferograms~~ were ~~inverted~~ generated using a Short Baseline Subset (SBAS) approach ~~to estimate the amplitude of~~. Displacement time series over the thaw season (June-September) are well fit with a linear model (RMSE scatter is less than 7 mm) and show maximum seasonal subsidence; ALT was estimated from the measured subsidence. of 20-60 mm. ICESat-2 products were used to validate the InSAR displacement time-series. ~~Most subsidence occurs~~ ALT was estimated from measured subsidence using a widely used model exploiting the volume difference between June ice and August water, reaching a maximum depth in our study area. ~~The maximum amplitude of seasonal subsidence was 2-6 cm, with ALT reaching ~ of 1.5 m.~~ Estimated ALT is in good agreement with in-situ and other remotely sensed data, but is sensitive to assumed thaw season onset, indicating the need for reliable surface temperature data. Our results suggest the feasibility of long-term permafrost monitoring with satellite InSAR. However, the C-band (~55 mm center wavelength) Sentinel radar is sensitive to vegetation cover, and in our studies was not successful for similar monitoring in the heavily treed discontinuous permafrost zone of Central Alaska.

1. Introduction

Permafrost is usually covered with soil or sediment – the active layer – which freezes and thaws seasonally. ~~This layer also moderates the impacts of surface temperature changes (Dobinsky, 2011).~~ The annual freeze-thaw cycle ~~of the active layer~~ causes significant surface height ~~changechanges~~ due to the volume difference between ice and liquid water. Active layer thickness (ALT) can be estimated ~~using simplified physical models and from the magnitude of~~ surface subsidence ~~measurements~~ during the thaw season using simplified physical models (Liu et al., 2012, 2014, 2015; Schaefer et al., 2015; Hu et al., 2018). ALT is expected to increase as Arctic temperatures rise and permafrost undergoes long-term thaw, ~~so remote monitoring of this feature is important.~~ releasing carbon dioxide and methane, both powerful greenhouse gases. The process thus represents a potentially powerful positive feedback in the global climate system (e.g. Schuur et al., 2009; Turetsky et al., 2020). On the other hand the active layer can also moderate the impact of surface temperature changes on deeper permafrost (Dobinsky, 2011), perhaps limiting rapid increases in ALT. Frequent monitoring of ALT across the Arctic landscape is clearly important, implying the need for remote sensing approaches.

In the last three decades satellite-based Interferometric Synthetic Aperture Radar (InSAR) has been used to monitor a variety of Earth processes that generate subtle surface displacements, including earthquake and volcano deformation, and reservoir compaction from fluid withdrawal (e.g., Bürgmann et al., 2000). Recent examples include earthquake after-slip (e.g., Sadeghi Chorsi et al., 2022a, b), volcano deformation (e.g., Poland and Zebker, 2022, Grapenthin et al., 2022), groundwater extraction (e.g., Castellazzi et al., 2016), carbon sequestration (e.g., Yang et al., 2015; Vasco et al., 2020), seismicity induced by fluid injection (e.g., Deng et al., 2020), coastal sea ice dynamics (Dammann, 2019)), glacier velocity estimation (e.g., Strozzi et al., 2020), and coastal flood hazard (e.g., Bekaert et al., 2017; Zhang et al., 2022). Pioneering work by L. Liu (Liu et al., 2010, 2012) demonstrated the

utility of InSAR to monitor long-term permafrost thaw and changes in ALT. Here, we use InSAR from the Sentinel-1 satellite constellation to investigate permafrost thaw on ~~the North Slope of Alaska for the period 2017 to 2022, focusing on multi-year changes in ALT,~~ part of the North Slope of Alaska for the period 2017 to 2022, focusing on multi-year changes in ALT, and using available ICESat-2 LiDAR data to validate the InSAR result. Our study has the following objectives: (1) examine the spatial distribution of seasonal thaw subsidence amplitude using SAR interferometry from 2017 to 2022; (2) use the annual variation of InSAR-measured displacements to estimate ALT and compare to long-term in-situ ALT observations; (3) assess the ability of the ICESat-2 ATL08 product to complement InSAR data in permafrost regions; and (4) test the influence of some environmental factors on the yearly variation of ALT.

2. Previous Work

Satellite remote sensing of permafrost has been ongoing for at least three decades (e.g., Peddle and Franklin (, 1993). ~~In terms of~~ Table-1 summarizes microwave-based studies, Singhroy et al. (2007) ~~used RADARSAT-1 to monitor permafrost activity and landslide motion around the Mackenzie Valley Pipeline Corridor, Canada. Rykhus and Lu (2008) used JERS-1 L-band data to detect thaw settlement over the Alaskan Arctic coastal plain. Liu et al. (2010) used ERS-1 and -2 SAR images to monitor permafrost on the North slope of Alaska, observing in three categories: 1) seasonal subsidence of ~1-4 cm and average secular subsidence of ~1-4 cm/decade. Liu et al. (2012) used SAR data to develop a novel ALT retrieval model, relating InSAR-derived subsidence to ALT using air temperature, soil texture, and organic matter thickness, assuming subsidence in a given thaw season is related to the volume reduction associated with the phase change between ice and water. We follow a similar approach in this study.~~

Schaefer et al. (2015) used ALOS PALSAR data from 2006-2010 to estimate average ALT thaw, 2) seasonal and long-term subsidence; and 3) ALT estimation and other scientific applications. Papers most relevant to this study include Liu et al. (2010, 2012, 2015), and Schaefer et al. (2015). in Barrow, Alaska. Their model showed good agreement between remotely estimated ALT, Ground Penetrating Radar (GPR) and in-situ data for more than 75% of the area. Daout et al. (2016) used multi-temporal InSAR observations to quantify ALT over Northwestern Tibet. They found that unconsolidated sediments in flat basins have higher seasonal subsidence amplitude compared to slope sediments and proposed that ground water was the key controlling factor. Iwahana et al. (2016) used InSAR data from ALOS PALSAR together with GPS data to study the long-term impacts of wildfire on the permafrost regime in the Anaktuvuk, Alaskan North Slope. Chen et al. (2018) used Sentinel-1 InSAR data to estimate seasonal thaw subsidence and inter-annual elevation change from 2016 to 2017 in Yedoma, Russia. They found that the top of the flat Yedoma upland exhibits large seasonal subsidence, and suggested that the delayed thaw season in 2017 was related to air temperature fluctuations. Strozzi et al. (2018) used Sentinel-1 InSAR to measure seasonal thaw subsidence in four sites, observing seasonal subsidence from 2 to 10 cm. Liu and Larson (2018) used GPS interferometric reflectometry (GPS-IR) at Barrow, Alaska, showing that surface elevation could be measured reliably during snow-free summer days. Hu et al. (2018) also used GPS-IR here, observing elevation changes with a seasonal amplitude of ~5 cm. Michaelides et al. (2019) used ALOS data to estimate seasonal subsidence, long-term subsidence and ALT to develop a fire response model. Bartsch et al. (2019) used Sentinel-1 (C-band) and COSMO-SkyMed (X-band) SAR images between 2013 to 2018 to monitor seasonal subsidence in central Yamal, Russia. Wang et al. (2020) used Sentinel-1 time-series in northern Canada, demonstrating the utility of C-band radar for monitoring ALT in a sub-arctic tundra region. Chen et al. (2020) used ALOS PALSAR data to monitor ALT in Toolik, Alaska. Honglei et al. (2021)

used ALOS PALSAR for the period 2007 to 2010 to permafrost-related subsidence in the Qinghai-Tibet Plateau, observing settlement up to 12 cm. Michaelides et al. (2021) and Chen et al. (2023) used L-band UAVSAR InSAR and AirMOSS P-band polarimetric backscatter data over different sites in Alaska and western Canada to simultaneously estimate seasonal subsidence, ALT and volumetric water content. Here, we use Sentinel-1 interferometry to monitor seasonal subsidence and ALT changes from 2017 to 2022 for part of northern Alaska. _____

-Table-1. Microwave-based studies on permafrost monitoring.

<u>Technical Application</u>	<u>Studies</u>	<u>Scientific Focus</u>	<u>Data</u>	<u>Study Area</u>
	<u>Singhroy et al. (2007)</u>	<u>Landslide and wildfire</u>	<u>RADARSAT-1</u>	<u>Mackenzie Valley, Canada</u>
	<u>Rykhus and Lu (2008)</u>	=	<u>JERS-1</u>	<u>Alaskan Arctic coastal plain</u>
	<u>Liu et al. (2010),</u>	=	<u>ERS-1 and ERS-2</u>	<u>North slope of Alaska</u>
	<u>Iwahana et al. (2016)</u>	<u>Thermokarst, wildfire</u>	<u>ALOS PALSAR, GPS</u>	<u>North slope of Alaska</u>
	<u>Strozzi et al. (2018)</u>	=	<u>Sentinel-1</u>	<u>Multiple sites in Alaska, Greenland, Russia and Antarctica</u>
	<u>Zwieback et al. (2018)</u>	<u>Thermokarst</u>	<u>TanDEM-X</u>	<u>Tuktoyaktuk coastlands, Canada</u>

<u>Seasonal Thaw</u>				<u>and Lena River delta, Russia</u>
	<u>Bartsch et al. (2019)</u>	=	<u>Sentinel-1 and COSMO-Skymed</u>	<u>Yamal, Russia</u>
	<u>Wang et al. (2020)</u>	=	<u>Sentinel-1, TerraSAR-X, ALOS PALSAR</u>	<u>Northern Canada</u>
<u>Seasonal and Long-term subsidence</u>	<u>Liu et al. (2012)</u>	=	<u>ERS-1 and ERS-2</u>	<u>North slope of Alaska</u>
	<u>Daout et al. (2016)</u>	=	<u>Envisat</u>	<u>Northwestern Tibet</u>
	<u>Chen et al. (2018)</u>	=	<u>Sentinel-1</u>	<u>Yedoma, Russia</u>
	<u>Liu and Larson (2018)</u>	=	<u>GPS-IR</u>	<u>Barrow, Alaska</u>
	<u>Hu et al. (2018)</u>	=	<u>GPS-IR</u>	<u>Barrow, Alaska</u>
	<u>Michaelides et al. (2019)</u>	<u>Wildfire</u>	<u>ALOS PALSAR</u>	<u>Yukon–Kuskokwim Delta, Alaska</u>
	<u>Chen et al. (2020)</u>	<u>Soil Moisture</u>	<u>ALOS PALSAR</u>	<u>Toolik, Alaska</u>
	<u>Bernhard et al. (2020)</u>	<u>Thermokarst</u>	<u>TanDEM-X</u>	<u>Northern Canada</u>
<u>Honglei et al. (2021)</u>	=	<u>ALOS PALSAR</u>	<u>Qinghai-Tibet Plateau</u>	
	<u>Liu et al. (2012)</u>	=	<u>ERS-1 and ERS-2</u>	<u>North slope of Alaska</u>
	<u>Schaefer et al. (2015)</u>	<u>Thermokarst</u>	<u>ALOS PALSAR</u>	<u>Barrow, Alaska</u>
	<u>Michaelides et al. (2019)</u>	<u>Wildfire</u>	<u>ALOS PALSAR</u>	<u>Yukon–Kuskokwim</u>

ALT estimation; other				<u>Delta, Alaska</u>
	<u>Chen et al. (2020)</u>	<u>Soil Moisture</u>	<u>ALOS PALSAR</u>	<u>Toolik, Alaska</u>
	<u>Michaelides et al. (2021)</u>	<u>Soil Moisture</u>	<u>L-band UAVSAR and AirMOSS P-band</u>	<u>Alaska and western Canada</u>
	<u>Chen et al. (2023)</u>	<u>Soil Moisture</u>	<u>L-band UAVSAR and AirMOSS P-band</u>	<u>Alaska and western Canada</u>

[Figure 1]

Figure 1 : DEM of including study area in northern Alaska. Solid (black box) in northern Alaska. Black box is expanded in Figure-1b, red box outlines boxes outline focused test area shown in Figure-5. Triangle Black triangle shows CALM site (U8) used to compare ALT, where ground-based measurements of ALT are available. Blue circle represents location of closest meteorological site used in this study station (Sagwon). (b): Line of sight (LOS) displacement of the study area from 2022-06-10 to 2022-09-02, as measured by InSAR. Negative values means mean displacement away from satellite, positive values mean displacement towards satellite. DEM relief map is shown in background. Triangles show location of CALM site and displacement time-series shown in Figure 3. Black square represents reference point used for InSAR analysis.

shown in background. Triangles show location of displacement time-series shown in Figure-3 and CALM site. Black square represents reference point for InSAR used in this study.

3. Study area

3. Study area

The Alaskan North Slope is bounded by the Brooks Range to the south and southeast and the Arctic Ocean to the north. Our main study area site on the North Slope is located in northern Alaska a 15 km by 30 km area in the vicinity of the Sag river and Dalton highway (69.68 N, 148.7 W; Figure-1). It is ~50 km south of Prudhoe Bay and ~130 km westnorth of the Brooks range. It is located Brooks Range, in the continuous permafrost region of Alaska with more than 90% permafrost coverage (Jorgenson et al., 2008). The

Our study site is described as having 23 cm organic layer thickness with seasonal high water table subject to saturation. The U8 includes CALM site's site U-8. The Circumpolar Active Layer Monitoring (CALM) program is designed to monitor the active layer and permafrost sensitivity to climate change over extended periods, typically spanning multiple decades (Brown et al., 2000). CALM site U8 has recorded ALT since 1996. The site encompasses a one-hectare area containing 121 sample square arrays, each measuring approximately 10 meters horizontally. It is located 88 m above sea level, is relatively flat, and lies within an inner coastal plain with river terraces. The site has an organic layer ~23 cm thick that is usually water-saturated during thaw season. U8's vegetation coverage is classified as graminoid-moss tundra, graminoid; prostrate-dwarf-shrub, and moss tundra. This site's landscape is described as inner coastal plain with river terraces. Its soil texture is classified as predominantly sand, gravel and peat. Soil taxonomy is Ruptic-Histic-Aquorthel (Ping et al., 2015; US Department of Agriculture, 1999), i.e., a poorly drained, occasionally to frequently water-saturated soil with a significant amount of organic matter. (https://www2.gwu.edu/~calm/data/webforms/u8_f.htm). A 12 km by 12 km test site around U8 (red

box in Figure 1) is used for focused studies of ALT estimation, based on our InSAR-derived displacement estimates during thaw season.

The Circumpolar Arctic Vegetation Map (CAVM) ~~describ~~eat this location describes graminoid and prostrate-dwarf-shrub vegetation ~~as~~5-10 cm tall in height. This ~~short~~vegetation structure is likely favorable for shorter radar wavelength radars ~~like Sentinel's~~such as Sentinel-1's C-band (~~(~5.5 cm wavelength ~5.5 cm)~~(~5.5 cm wavelength)) to retain phase coherence. ~~For comparison we also studied the Beta site of the APEX (Alaska Peatland EXperiment), located approximately 30 miles southwest of Fairbanks (64.696 N, 148.322 W). This is a located in discontinuous permafrost zone with abundant black spruce, up to 5 m in height., but also suggests that accounting for vegetation height will be important to assess seasonal and longer term elevation changes in this area.~~

4. Methods

4.1. InSAR Data Processing

4.1.1. Data and Material

~~Sentinel-1 SAR images from June to September 2017 to 2022 were selected to cover the end of freeze season to the end of thaw season (Table-S1). Changes in surface scattering characteristics in the freeze season (surface covered with snow and ice) could decorrelate the radar wave. Significant changes in scattering characteristics are expected during the freeze season when the surface is covered with snow and ice, hence we focus on the summer thaw season. Changes in soil moisture in any season could also decorrelate the radar wave, but terrain in the continuous permafrost zone is saturated at the beginning of thaw season and is likely to remain so for most of the remaining thaw season as the permafrost layer~~

continues to melt. We focused our study on the June to September time frame, using Sentinel-1 SAR images with a 12 day revisit interval and descending geometry for the years 2017 to 2022 (Table-S1).

We used the Alaska Satellite Facility's Hybrid Pluggable Processing Pipeline (HyP3) software to form interferograms (Hogenson et al., 2020). HyP3 uses the Copernicus GLO-30 Digital Elevation Model (DEM) for scene ~~coregistration~~co-registration and topographic phase corrections (ESA., 2021). Interferograms were filtered using the adaptive phase filter in Goldstein & Werner (1998). Individual interferograms were unwrapped using a minimum-cost-flow algorithm (Chen & Zebker., 2002) and geocoded to a 30-m grid spacing. We used the open-source Miami InSAR time-series software in python (MintPy) to generate LOS displacement time-series from the unwrapped and geocoded interferograms (Fattahi et al., 2016; Zhang et al., 2019). Interferograms with high spatial coherence and short time-interval between scenes were chosen to avoid decorrelation and phase unwrapping errors. Phase unwrapping artifacts occur in permafrost regions when disconnected wetlands and large seasonal deformation precludes smooth unwrapping of the phase (e.g., Strozzi et al., 2018). Noisy interferograms were removed from the time-series and seasonal amplitude inversion processes (Section 4.3.2). Geocoded LOS displacement data for active layer thickness estimation was then extracted for the study area.

4.1.2. Reference Point Selection

~~InSAR is a double-difference technique that~~InSAR measures phase differences between SAR observations in space and time. To relate these phase difference measurements to surface displacement, ~~we need to choose~~ a reference location with assumed or known displacement. It is required, with high temporal coherence (> 0.8) to avoid introducing noise into the time series. In most permafrost regions,

rock outcrops are a suitable good reference locations—as they can be assumed to show only minimal displacement, but. However, they may not be available for all regions. For this study, we use two criteria for reference point selection: first, we require the point to have high temporal coherence (> 0.8) to avoid introducing noise into our time series. Second, we look for locations that either are rock outcrops or lie in a floodplain (but not a river channel, which can undergo large elevation changes from erosion/deposition events; see Figure S1). Liu et al. (2010) point out that river floodplains usually have well-drained sandy soils and hence tend not to experience significant frost heave. They may be used as reference points if they are not within a river channel, which can undergo large elevation changes from erosion/deposition events (see Figure S1). Figure 1b shows the our reference point we identified using these criteria, a rock outcrop immediately northeast of our study area which remains coherent (temporal coherence ~0.95) during the 2017 to 2022 thawing thaw seasons.

4.1.3. Atmospheric delay correction

Atmospheric effects are one of the main error sources in the InSAR process (Meyer et al., 2006). While InSAR data can be affected by both the ionosphere and the troposphere, here we focus on tropospheric effects as ionospheric impacts are less pronounced in C-band data (Meyer ~~et al.~~, 2011). Tropospheric phase impacts can be modeled as (Ding et al., 2008):

$$\Delta\phi = \phi_2 - \phi_1 = \frac{4\pi}{\lambda}[d_2 - d_1] + \frac{4\pi}{\lambda}[\delta d_2 - \delta d_1] \quad (1)$$

where ϕ is the phase of a SAR image, d is the range from satellite to surface, δd is the tropospheric propagation delay, and λ is the radar wavelength. Tropospheric phase signals in InSAR data can be caused by two processes: changes in the atmospheric stratification and turbulent mixing. The stratified phase component typically correlates with topography (Hanssen, 2001) and may be estimated and then removed based on delay-elevation correlations, then removed from the radar phase (Doin et al., 2009).

The turbulent component ~~plays an important role in phase delay because it is uncorrelated in time and space, although its amplitude is usually~~ much less than the stratified component, ~~but is uncorrelated in time and space and hence harder to predict or measure~~. According to (1) if the atmospheric propagation conditions at the time of SAR acquisitions are not the same ($\delta d_2 - \delta d_1 \neq 0$), then tropospheric phase components will be introduced, contaminating the true displacement signal. ~~To reduce these tropospheric effects, one approach is to apply a global weather model. This approach mainly reduces the stratified component.~~ Applying atmospheric corrections to C-band radar images can improve signal to noise ratio, especially when there is a considerable height difference between the study area and reference point. We applied the atmospheric correction model described in Jolivet et al. (2011, 2014) using ECMWF reanalysis (ERA-5) datasets (Hersbach et al., 2020). This approach mainly reduces the stratification component of the tropospheric delay.

4.2. ICESat-2 data processing

~~We used the ICESat-2 level 3A product for land and vegetation height (ATL-08) to validate the InSAR time-series displacement estimates. While the nominal temporal resolution of ICESat-2 data is 91 days, cloud cover greatly limits the amount of usable data in Alaska (e.g., Neuenschwander & Pitts., 2019). Two observations were available in our study area, acquired on 2021-06-08 and 2021-09-06.~~ To validate our InSAR measurements of thaw season subsidence, we used independent LiDAR elevation data from the ICESat-2 satellite (Martino et al., 2019). The ATLAS (Advanced Topographic Laser Altimeter System) LiDAR on ICESat-2 uses a multi-beam photon-counting laser operating at 532 nm, i.e., the green portion of the electromagnetic spectrum. Surface range is determined by the travel time of each detected photon. When coupled with the satellite's position, the range data provides accurate geolocation of the surface, in this case referenced to the WGS-84 ellipsoid. With a laser repetition rate

of 10 kHz, pulses occur approximately every 70 cm on Earth's surface. Each footprint is about 13 m in diameter. Beam pairs, with different energies to adjust for surface reflectance, are spaced about 3.3 km apart across tracks, forming six tracks with beams in each pair separated by 90 m. Ranging precision for flat surfaces is expected to have a standard deviation of around 25 cm, primarily influenced by ATLAS timing uncertainty (Neuenschwander et al., 2019).

The ATL08 product algorithm is designed to extract terrain and canopy heights from vegetated surfaces using the geolocated photons (Neuenschwander et al., 2019; 2021). We used the 'h_te_best_fit' parameter, which estimates terrain height by fitting a plane to along-track points in each 100 m segment and ~~report the height of the middle of the fitted plane (Neuenschwander et al., 2019; 2021).~~ ~~Due to pointing-related errors~~ reports the height of the middle of the fitted plane (Neuenschwander et al., 2019; 2021), reducing the impact of random errors. The height of the terrain midpoint is calculated by choosing the best fit among three models: linear, third-order, and fourth-order polynomials applied to the terrain photons. This allows for interpolation of the elevation at the midpoint of the 100-meter segment (Neuenschwander et al., 2019; 2021, Neuenschwander and Pitts, 2019). The standard deviation of terrain points around the interpolated ground surface within the segment is one measure of surface roughness. Neuenschwander et al., (2019) provide additional details describing the ATL08 algorithms. ATL06 is an alternate product algorithm, optimized for ice surfaces, and has been used in some permafrost studies (e.g., Michaelides et al., 2021) (See Supplement).

While the nominal temporal resolution of ICESat-2 data is 91 days, cloud cover often limits the amount of usable data in Alaska (e.g., Neuenschwander & Pitts., 2019). Two repeat track observations were available in our study area, acquired on 2021-06-08 and 2021-09-06. Due to pointing-related

uncertainty, observations are not always repeated in expected locations, which amplifies the height uncertainty. To address this issue, we divided the study area into 50 m grid cells, and assigned each observation in 2021-06-08 and 2021-09-06 repeat tracks to one of those grid cells. Figure-S1 shows the height difference between all reported terrain observations in the study area between 2021-06-08 and 2021-09-06. In the limited area where both InSAR and ICESat-2 data are available (~~four points shown in Figure 1a~~), we used the ICESat-2 data to evaluate the compare to our InSAR results (Figure 3 and Supplement).

4.3. ~~ALT~~ Active Layer Thickness estimation model

To relate the InSAR observations to ALT, we assume that the measured LOS displacements are predominantly due to vertical motion (negligible horizontal motion) and that this vertical motion is caused by thawing ground ice in the active layer. The assumption of negligible horizontal motion is justified because over the short data time interval is short and the technique does is not sensesensitive to long-term tectonic motion. ~~We observed large displacements in~~ Displacements from the M 6.4 August 2018 earthquake, ~130 km east of study area ~~due to the M 6.4 earthquake~~ (USGS hypocenter at north of Brooke range: 145.291 W, 69.576 N, depth 15.8 km). ~~Since our study area was far from this area, we believe most of~~ are negligible. Most surface motion in the deformation in thaw season is because of therefore likely reflects thawing ground ice ~~thawing~~. We project the LOS displacements into the vertical direction using the local incidence angle (θ) for each radar pixel (see Equation-3). We follow the simplified Stefan solution to estimate depth of thawing in the soil (Nelson et al., 1997) aided by field-observed air temperature data. We also assume that subsidence can be related to a simple thaw index, for example the accumulated degree days of thawing (ADDT). Our procedures are virtually identical to those

described in Liu et al. (2012) and Schaefer et al. (2015), with the exception that we do not estimate multi-year subsidence and do not average ALT across multiple thaw seasons. This enables us to directly compare our space-based estimates with yearly ground truth estimates from CALM site U8 and evaluate inter-annual changes in ALT.

4.3.1 ~~ADDT~~ Accumulated Degree Days of Thawing calculation

To calculate ADDT, we use the NOAA Climate Data Online (CDO) tool to find nearby meteorological stations. The closest station is ~2030 km south to our studytest area (Name: Sagwon, Figure 1a). We assume that our studytest area has the same temperature trend as this station ~~from~~for the 2017 to 2022 thaw seasons. We define the first and last day with temperature > 0 °C as the first and last day of the thaw season. ADDT is defined by the following equation (Riseborough., 2003):

$$ADDT = \int_0^{\alpha_s} (T_s - T_F) dt \approx \sum_0^{\alpha_s} \bar{T}_s \quad (2)$$

where α_s is the duration of thawing season, in days. T_s is surface temperature (°C), T_F is equal to freezing point, 0 °C, and \bar{T}_s is daily mean surface temperature. Due to lack of in-situ surface temperature data, we set T_s using air temperature observations.

4.3.2 Seasonal Amplitude Inversion

The relationship between the seasonal vertical surface displacement magnitude and ADDT can be written as (Liu et al., 2012; Schaefer et al., 2015):

$$D_i = \frac{LOS}{\cos(\theta)} = E(\sqrt{A_{2,i}} - \sqrt{A_{1,i}}) + \varepsilon \quad (3)$$

where D_i is the vertical displacement estimate for a given pixel in the i^{th} interferogram, θ is the local incidence angle at that pixel calculated from nadir, E is the amplitude of the seasonal vertical displacement estimate which reflects physical parameters such as soil thermal conductivity, latent heat

of fusion, soil density and relative water content: (Nelson et al., 1997). $A_{1,i}$ and $A_{2,i}$ are normalized accumulated degree days of thawing at the first and second acquisition date. ε is an error term that captures model deficiencies, noise, and other unknown error sources. We do not consider secular (long-term) displacement signals in (3) because we analyze the thaw seasons of 2017 to 2022 separately. This is the major difference between our approach and those described in Liu et al. (2012), Schaefer et al. (2015) and Michaelides et al. (2019), where seasonal and interannual trends were estimated simultaneously.

We can rewrite (3) in matrix form, considering the interferograms listed in table-S1, to estimate E using least squares: for separate thaw seasons:

$$\begin{bmatrix} D_1 \\ D_2 \\ \vdots \\ D_N \end{bmatrix} = \begin{bmatrix} \sqrt{A_{2,1}} - \sqrt{A_{1,1}} \\ \sqrt{A_{2,2}} - \sqrt{A_{1,2}} \\ \vdots \\ \sqrt{A_{2,N}} - \sqrt{A_{1,N}} \end{bmatrix} [E] \quad (4)$$

4.3.3 ALTActive Layer Thickness Inversion

If we assume that the seasonal vertical surface displacement amplitude E is caused only by thawing ice and corresponding volume reduction, we can write E as a function of physical properties such as soil porosity, soil moisture fraction, and density of ice and water through a vertical profile from surface to depth of the active layer (Liu et al., 2012; Schaefer et al., 2015):

$$E = \frac{\rho_w - \rho_i}{\rho_i} \int_0^{ALT} P(z)S(z)dz \quad (5)$$

The variables ρ_w and ρ_i in Eq(5) are the density of water and ice [kg m^{-3}], respectively. $P(z)$ is the soil porosity which is a function of depth and depends on soil content, and $S(z)$ is the soil moisture fraction of saturation. Here, Following Schaefer et al. (2015), we assume that $S(z) = 1$, which means

that the active layer is fully saturated and does not change with depth (Schaefer et al., 2015). In the next section, we describe relation between porosity in depth and ALT in (5).

4.3.4 Porosity Model

Following earlier authors, we assume the soil in the active layer consists of organic matter and mineral soil. In this case, the, with porosity decreases decreasing exponentially with depth due to decreasing organic matter. There is one active CALM site inside in our study test area: U8 (Figure 1a1b). This site is described as having 23 cm organic layer thickness, consisting mainly of peat plus sand and gravel (https://www2.gwu.edu/~calm/data/webforms/u8_f.htm). We consider this organic matter thickness in modeling of porosity versus depth. (Section 3). We applied the formulation introduced by Liu et al (2012) and presume assume that $P(z)$ is the weighted average of organic and mineral matter:

$$P = f_{org}P_{org} + (1 - f_{org})P_{mineral} \quad (6)$$

where P is the porosity, and f_{org} is defined as the organic soil fraction by Schaefer et al., (2009) as:

$$f_{org} = \frac{M_{org}}{M_{org-max}} = \frac{\rho_{org}}{\rho_{org-max}} \quad (7)$$

In Eq (7), M_{org} and ρ_{org} are the simulated mass of organic matter and organic soil density in a given layer of soil, respectively. $M_{org-max}$ and $\rho_{org-max}$ are bulk organic matter mass and bulk density for pure organic soil, respectively. We set $P_{org} = 0.95$ based on model from Bakian-Dogaheh et al. (2022). The porosity of mineral soil then depends on the sand fraction of soil. To estimate $P_{mineral}$ we utilized used the porosity-sand fraction relation provided in Liu et al., (2012):

$$P_{mineral} = 0.489 - 0.00126f_{sand} \quad (8)$$

We used Global Land Data Assimilation System (GLDAS) soil parameters with 0.25 degree spatial resolution to extract the soil sand fraction (Rodell et al., 2004). We set $P_{mineral} = 0.488$, and $\rho_{org-max}$

= 130 kg m⁻³ for bulk density of peat (Grigal et al., 1989; Hossain et al. 2015). As mentioned earlier, to formalize ρ_{org} with depth, we assume the organic matter amount decreases exponentially with depth:

$$\rho_{org} = A \exp(-kz) \quad (9)$$

where k is an empirical constant (m⁻¹), set to 5.5 (Liu et al., 2012; Jackson et al., 2003). To retrieve A , we use simulated mass of organic matter (M_{org} : total soil carbon content) from Johnson et al. (2011) and Mishra et al. (2012) and ensure that total carbon mass is conserved.

$$\int_0^{root} A \exp(-kz) dz = M_{org} \quad (10)$$

We set $M_{org} = 70$ kg m⁻² (Johnson et al., 2011; Mishra et al., 2012). The spatial divergence of total soil carbon content for the 0-100 cm depth range is large in Arctic tundra regions considering vegetation type. Mishra et al. (2012) and Johnson et al. (2011) ~~estimated~~ M_{org} estimate total soil carbon around our study area at [60-80] and [50-70] kg m⁻², respectively. Root depth is the maximum observed ALT at a given site since roots cannot penetrate solid ice. Here, we set maximum root depth at 1.1 m because maximum observed ALT at site U8 is reported as ~1.1 m for 2022. Then we solve (10) for A and replace it in (9). Figure 2 shows the relation between porosity and depth in a mixed soil. We set porosity=0.95 for the first ~2023 cm depth reflecting organic matter thickness. After 2023 cm depth, the porosity decreases exponentially, reaching its minimum near the top of the frost table. Finally, we put all equations into (5) and use a numerical bisection algorithm to solve for the upper integral limit, ALT. We set the accuracy of bisection to be at the mm level.

~~Finally, we put all equations into (5) and use a numerical bisection algorithm to solve for upper integral limit, ALT.~~

[Figure 2]

~~We set the accuracy of bisection to be at the mm level.~~

Figure 2. Depth-porosity model used in this study assuming a mixture of organic and mineral matter.

5-

Results and Discussion

5.1 Estimating Seasonal Vertical Displacement

Figure 3 shows displacement time-series for the four test locations shown in Figure 1b. All four locations show subsidence during thaw season. The maximum amplitude of subsidence ranges from 20 mm (Location 4) to 60 mm (Location 1). In 2021 the subsidence amplitude was small and similar among the four locations (~20 mm). The subsidence rate is approximately constant during the thaw season. The root mean square error (RMSE) of the linear fit to the displacement data is less than 7 mm at all four locations over all six years. The maximum subsidence rate observed during the short (~3-4 month) thaw season is ~18 mm/month.

Note that we do not attempt to connect our displacement time series across adjacent years. The freezing process, consequent frost heave, and deep snow at these sites during winter makes phase connection difficult due to loss of coherence (e.g., Strozzi et al., 2018). Nevertheless, our approach can still be used to assess long term (multi-year) changes in permafrost, as shown in Section 5.3.

Figure 4 shows the seasonal subsidence rates at the four locations over the six-year test period. No clear long-term trend is observed. Location (1) has the largest rate variation, from 4 mm/month in 2018 to 18 mm/month in 2020. Location (3) has the minimum rate variation, 5 mm/month in 2017 to ~10 mm/month in 2021. We do not observe spatial correlation between subsidence rates at the various locations. For example, location (1) shows the fastest subsidence, with high rates in 2017, 2020 and 2022 but much smaller rates in 2018, 2019 and 2021. Location (2)'s fastest subsidence occurs in 2019 while the fastest rates for location (3) and location (4) occurred in 2019 and 2021.

5.2 Validation of InSAR Surface Displacement Estimates with ICESat-2 Data

We used the ICESat-2 ATL-08 products data product to evaluate compare with our InSAR time-series results. We found four locations in common between ICESat-2 and InSAR data of relative height change for the 2021 thaw season; (Figure 3). Comparisons using the optical LiDAR data are primarily limited by cloud cover (Figure S1). Unfortunately, there were no, however all four of our test locations had suitable ICESat-2 comparison data for 2019, 2020 and 2022 thaw season. ATL-08 reports surface height relative to the WGS84 datum since mid-2018. To compare with relative InSAR data, we subtracted the two available ICESat-2 height data and assign at the beginning and end of the 2021 thaw season. To minimize the effect of systematic errors, we used repeat data from the same reference ground track, and considered only elevation change during thaw season, referencing the height of the second acquisition (end of thaw season; 2021/09/06) to the first (beginning of thaw season;

2021/06/08). The height of the first date's height as LiDAR data is assigned 'zero elevation.elevation', to agree with the InSAR estimate. This is a reasonable assumption because the two datasets have comparablesimilar start dates in 2021, June 8 for ICESat-2, and June 3 for SAR.


Figure 3 shows that with these assumptions, the LiDAR and radar approaches agree well. Since the two approaches to elevation change estimation are independent, their agreement is a strong validation of the InSAR approach, albeit limited to a small number of test cases.

The agreement between the two approaches agree well. This indicatesalso suggests that our reference point for the InSAR data experiences negligible change during the study period. Reference point selection for InSAR is difficult in remote permafrost regions as most area-subsideareas undergo subsidence during the thaw season. Comparing InSAR displacement with reliable and available ICESat-2 data when available could be an option to evaluate result in remote areas. However, finding suitable repeated ICESat-2 points is also difficult because of LiDAR help in this regard, but will be limited by pointing errors, cloud cover, and density of the vegetation canopy density. The chosen locations for comparison here are less than 50 m distant and have less than 7% slope.

We also tested the utility of ICESat-2's ATL06 data product ("h li"; Smith et al., 2019), described in the Supplement. For this test, we expanded the comparison to a larger number of sites and dates, but otherwise used the same general procedures as for the ATL08 product. For our original four test sites, the ATL08 product shows better agreement with the InSAR data (Figure S5). In our larger study area, 78 cells reported both ATL08 and ATL06 data. For these cases, the two products are equivalent (within 1 cm height difference-) in 9% of cases, and agree within 10 cm in 61% of cases (Figure S6). Including the four original test sites described above, for the 15 cases where InSAR and ICESat-2 products were available, ATL08 shows better agreement with InSAR in 8 cases, while ATL06 shows better agreement in 7 cases. In relatively flat areas, both data products show similar performance. The larger footprint of

the averaged ATL08 data product (100 m) compared to ATL06 (40 m) may also be advantageous given the high spatial variability of ALT (see section 5.3). The Supplement also includes a description of the formal uncertainties associated with both the ATL06 and ATL08 data products.

[Figure 3:]

Figure 3.  InSAR displacement time-series for four test locations (black triangles in Figure-1b) with respect to the first SAR acquisition in the thaw season. Black dashed lines are best-fitting regression lines for InSAR LOS displacement only. Rate and RMSE of fitted lines are shown in the top-left of each sub-figure. Red squares in 2021 show ICESat-2 ATL-08 terrain height product. Latitude and longitude of each analyzed location are shown in the bottom-left of each panel. Note that subsidence only occurs during the thaw season and not the entire year.

~~location are shown in the bottom-left of each panel.~~

[Figure 4]

Figure 4. Rate comparison of LOS displacement ~~between selected points during the summer thaw season for the locations~~ shown in Figure-1b. Rate and an error bar are from fitted linear ~~line (See Figure-3).~~

~~line (See Figure-3).~~

5.2. Estimated Seasonal Vertical Displacement and ALT

~~Figure 3 shows time-series for the four locations shown in Figure-1b. The maximum amplitude of subsidence for these locations ranges from 2-6 cm. Location (4) and location (1) have the minimum and maximum subsidence amplitude in the entire time-series. Most subsidence occurs in the first two months of data acquisition (Mid-June to mid-August) for all locations. The subsidence amplitude is similar between the four locations (up to ~2 cm) in 2021. The maximum rate of subsidence is ~20 cm/yr and the rate is approximately linear for most locations, with a root mean square error (RMSE) of the linear trend of less than 1 cm for all four locations from 2017 to 2022.~~

~~Figure 4 shows the subsidence rate change at the four locations over six years. No clear long-term trend is observed. Location (1) has the largest rate variation, from 5.7 in 2018 to 22.4 cm/year in 2020. Location (3) has the minimum rate variation, 7.1 in 2017 to 11.7 cm/year in 2021. We do not observe correlation between subsidence rates at the various locations. For example, location (1) shows the fastest subsidence, with high rates in 2017, 2020 and 2022 but much smaller rates in 2018, 2019 and 2021. Location (2)'s fastest subsidence occurs in 2019 while the fastest rates for point 3 and 4 occurred in 2019 and 2021.~~

5.3. Active Layer Thickness Estimation and Validation

Figure 5 shows the seasonal vertical displacement amplitude and its RMSE calculated from equation (4) and estimated ALT from 2017 to 2022 in our test area (red box in Figure-1a). The shallowest overall 1) using procedures described in Section 4.3. Minimum ALT in this area occurred in 2018 and 2021. The deepest Maximum ALT occurred in 2019 and 2020. The variation in these estimates may in part reflect uncertainty in thaw season length. Thaw season usually starts around May 20 and ends around September 20, but the accumulated degree days differ each year. Sagwon station data for this time period shows that the maximum and minimum ADDT occurred in 2019 and 2018, respectively (Table-3). The overall pattern of ALT remained the same in 2017, 2018, 2021 and 2022, but differed in 2019 and 2020. Maximum ALT occurred west and west-south of site U8. This was also true in 2019 and 2020 but spatial variation was higher than other years.

ALT in some areas showed a deeper-than-usual pattern in 2019 and 2020, but recovered in 2021 and 2022. For example, an area a few kilometers south-east of U8 showed high variability in 2019 and 2020, but shallow ALT before (2017 and 2018) and after (2021 and 2022). Deeper ALT in 2019

correlates with ADDT. However, deeper ALT in 2020 and shallower ALT in other years does not clearly correlate with ADDT — 2020 was the second coolest thaw season in our study period with ADDT = ~876 °C days (Table-3).

Table–3: Thaw onset, end and ADDT for 2017 to 2022 based on Sagwon station (Figure 1).

<u>Year</u>	<u>Thaw onset [m / d]</u>	<u>Thaw end [m / d]</u>	<u>ADDT [°C day]</u>
<u>2017</u>	<u>5 / 24</u>	<u>9 / 19</u>	<u>980.8</u>
<u>2018</u>	<u>6 / 12</u>	<u>9 / 21</u>	<u>713.5</u>
<u>2019</u>	<u>5 / 20</u>	<u>9 / 14</u>	<u>1040.2</u>
<u>2020</u>	<u>5 / 21</u>	<u>9 / 19</u>	<u>875.7</u>
<u>2021</u>	<u>5 / 21</u>	<u>9 / 17</u>	<u>943.5</u>
<u>2022</u>	<u>5 / 19</u>	<u>9 / 21</u>	<u>970.8</u>

[Figure 5]

Figure 5. Estimated seasonal amplitude, its RMSE and ALT for study area (red box Figure-1a) from 2017 to 2022. Black triangle shows location of CALM site U8. White areas represent low coherence which are masked out in the model calculations. The Sag river runs south to north in the center of each panel (See Figure-S1).

5.3. ALT Evaluation


We can compare our results with in-situ data. CALM site U8 is a one hectare area with 121 samples in a square array. Each array has a 10x10 m length. Its ALT has been observed at the end of the thaw season since 1996. Thaw depth is measured by pushing a metal rod into the soil to refusal, assumed to represent the top of the permanently frozen layer. The ALT is not reported whenif the arrayprobe intersects large pondsponded water or rocks. The mean of all 121 ALT measurements and therethe corresponding RMSE are reported. Our approach for reporting the InSAR-derived ALT is similar.  averaged ALTThe pixel to closest to U8 and adjacent pixels with within 50 m in the center of closest pixel to U8, a radius of 100 m, and calculated east-west and north-south directions are defined. We report the corresponding RMSEmean of these pixels and their RMSE for comparison with in-situ data.

Figure 6 shows ALT data around the U8 CALM site for different years. Our estimated ALT agrees within uncertainty with the in-situ data infor all five of the years, 2017, 2018, 2019, 2021 and 2022 (Table-1). when data is available. In-situ ALT is not reported for 2020.

Chen et al. (2022) estimated ALT and volumetric water content for large areas in Alaska coveringincluding the U8 CALM site using L-band UAVSAR and AirMOSS P-band polarimetric SAR, respectively. Their result is in reasonablegood agreement with the in-situ data and this study considering joint uncertainties. Data processing details are provided in Michaelides et al. (2022) and Chen et al. (2023). Table-1 shows a summary of the ALT comparison.

Table1. Estimates of ALT at CALM site U8. ‘ND’ means no data available.

Year	This Study	CALM (U8)	Chen et al. (2022)
2017	60.9 ± 33.5	68.9 ± 11.7	49 ± 17

2018	70.7 ± 41.5	61.7 ± 11.7	ND
2019	73.7 ± 31.7	70.3 ± 12.1	ND
2020	98.5 ± 8.5	ND	ND
2021	76.7 ± 18.9	60.8 ± 9.7	ND
2022	58.7 ± 22.4	65 ± 12.1	ND

Our results and in-situ data suggest that ALT exhibits high spatial variability, perhaps reflecting local variability in topography or soil moisture. Since soil moisture reflects in part local topographic variation, measuring ground elevation to high precision may be important to understanding this variability.

[Figure 6]

Figure 6. ALT comparison at CALM site U8. Blue triangles represent average in-situ ALT from manual mechanical probing across all grid cell from 1996 to 2022 (<https://www2.gwu.edu/~calm/data/north.htm>). Green circle is estimated ALT for the closest pixel to U8, using airborne L- and P-band SAR images (Chen et al., 2022). Red squares (this study) are average estimated ALT for pixels with 100 ± 50 m distance to U8. In-situ ALT is not reported for 2020.



Assess the agreement between in-situ data and estimated ALT, we follow Liu et al. (2012) and use equation 11 to evaluate whether a given year's InSAR-based estimate of ALT is consistent with the in-situ observation given its data uncertainty:

$$r^2 = \left(\frac{ALT_{Mod} - ALT_{Obs}}{\sigma_{Obs}} \right)^2 \quad (11)$$

where the numerator is the residual between in-situ and InSAR-based ALT, and the denominator is the reported in-situ data uncertainty. r^2 values lower than 1 indicate good agreement. Except for the 2017 estimate, with $r^2 = 2$, all other years have r^2 less than 1. Estimated ALT in 2022 show the best agreement with $r^2 = 0.3$. Figure S4 gives more details.



Our results and the in-situ data suggest that ALT exhibits high spatial variability. It is generally assumed that ALT depends on parameters such as ADDT, precipitation, and local topography, the latter reflecting its influence on soil moisture and aspect. Our results show a moderate correlation with ADDT but no correlation with precipitation, although the latter could reflect limited spatial resolution of the available data.

The influence of local topography on ALT can be tested by examining available high resolution in-situ data. Data from the U8 CALM site provides an excellent opportunity to investigate both spatial and temporal variability of ALT. Over this small area we expect that local topography will show minimal year to year variation. Figure 7 shows ALT variation over an 11x11 square array of sample points, with each point sampling an area of 10x10 m. Data are available for the period between 1996 and 2022 with a gap in 2020. Location is described in local coordinates. We also show the RMSE of each grid point from its average over this time period, and a time series of ALT for three representative points in the array.

Even over this small area we see no significant spatial or temporal pattern in ALT over the quarter-century period of available data. At least for this example, the influence of local topography appears to be minimal, although we cannot preclude microtopographic (less than 10 m) effects that vary over time.

The Mann-Kendall test was employed to evaluate this in a rigorous way. The test determines if a significant monotonic trend is present for either increasing or decreasing ALT at each grid point. Data spanning from 1996 to 2019 were analyzed due to the absence of data in 2020. To maintain consistency and account for possibly significant temporal variation in ALT, data from 2021 and 2022 were excluded. The null hypothesis was rejected for 31.4% of the cells; the remaining 68.6% of cells do not show a statistically significant trend. In other words, only 38 out of 121 cells had a significant increasing or decreasing ALT trend. Among these 38 cells, 35 cells showed an increase in active layer thickness over the sample time period. The maximum RMSE of the cells is ~20 cm. Variation of the same grid cell in two consecutive years reaches as high as ~60 cm. Since air temperature (related to ADDT) and precipitation are unlikely to vary significantly over this 100x100 m area, and since overall morphology is unlikely to vary significantly over this time period, other factors must explain the variation in ALT. Micro-topographic effects, temporal changes in sub-surface moisture flow, soil organic content and vegetation growth and decay are possible factors. Nelson et al. (1998), Nelson et al. (1999), Hinkel and Nelson (2003) conclude that in-situ ALT shows Markovian behavior with high spatial and temporal variation.

[Figure 7]

Figure 7. ALT variation of CALM site U8, RMSE of each cell relating to its annual average from 1996 to 2022, ALT trend and ALT time-series for three selected cell (10x10 m) shown by white star.

5.4. Relation of meteorological parameters ~~and ALT~~ to Active Layer Thickness

We investigated correlations between in-situ ALT and several meteorological parameters, including ADDT and precipitation in thaw seasons from 2002 to 2022. -ADDT and precipitation data are from the Sagwon meteorological station. Figure [7a8a](#) shows the relation between ADDT and ALT. From Stefan's equation, we expect a positive correlation between ADDT and ALT. -However, the correlation is statistically weak (R-squared = 0.42; Figure [7b8b](#)) suggesting the influence of additional factors. Precipitation may influence ALT, e.g., by advecting heat downward to promote permafrost thaw, but there are additional factors to consider. For example, an increase in soil moisture leads to a rise in the thermal conductivity of soil, potentially increasing the depth of the active layer during thaw season. However, an increase in soil moisture also increases the total amount of heat required for thawing, promoting a shallower active layer. Clayton et al. (2021) showed that ALT has a positive correlation with volumetric water content (VWC) in the upper 12 cm of soil, a negative correlation with bulk VWC, and no statistically significant correlation with VWC in the upper 20 cm of soil. We also do not see a statistically significant correlation between ALT and precipitation, presumably perhaps reflecting these opposing impacts (Figure [7e](#)).

[8c](#)). We also used simple regression analyses to relate ALT to several multi-parameter factors including ADDT, precipitation and accumulated degree days of freezing (ADDF) from the previous year. However, these did not improve the correlation. Perhaps other factors such as local elevation gradients (influencing local hydrology), vegetation type, or the previous year's snowfall need to be considered. It is also possible that some of the variability in our ALT estimates reflects instead variations in total ice content (Zwieback et al., 2024).

[Figure 78]

Figure 8. (a): Relation between ADDT and ALT from 2002 to 2022 in CALM site U8 and Sagwon station. Red circles show ADDT. Blue triangles show in-situ ALT. (b) scatter plot of ALT vs ADDT. (c) scatter plot of ALT vs precipitation. R-squared of relation is shown in top-left of panels. ADDT and precipitation are calculated from ~~first of~~ June 1 to ~~first of~~ September 1 of each year to be consistent with ALT measurements.



5.5 Applicability to other regions

Alaska's North Slope is an optimum region for InSAR-based approaches to permafrost monitoring because of limited tree cover. We also tested our technique in a region with more extensive tree cover, the Beta site of the APEX (Alaska Peatland EXperiment) project, located approximately 30 miles southwest of Fairbanks (64.696 N, 148.322 W). This site is located in Alaska's discontinuous permafrost zone and has abundant black spruce, up to 5 m in height. The technique was not successful, as phase coherence was not maintained in successive SAR images, perhaps reflecting the relatively short wavelength (C-band) of the Sentinel-1 SAR instrument (see next section). Average spatial and temporal coherence maps for these two sites are compared in Figure S1.

5.6 Limitations and Future Research

Four aspects of our ~~model may~~approach limit its utility: and are an obvious focus for future research.


1. Decorrelation of InSAR phase is the main limitation of ~~this our~~technique. Accurate InSAR measurements require a high degree of coherence, a measure of the correlation in radar phase between

the two SAR images. Decorrelation occurs due to temporal changes in surface scattering properties, changes in viewing angles, and noise in the SAR data (e.g., Schaefer et al., 2015). C-band InSAR has demonstrated its ability to monitor deformation over continuous permafrost region at higher latitudes (see Previous Work, [and this study](#)). Wang et al. (2020) compared the efficiency of Sentinel-1 for monitoring permafrost deformation in discontinuous permafrost regions. They concluded that Sentinel-1 InSAR time-series performs effectively over ~~discontinuous~~ permafrost landscapes mainly beyond the tree line, such as tundra, tundra wetlands, and less developed shrub-tundra areas, ~~during thaw season.~~ However, the outcomes and precision are less favorable in shrub-tundra and forest-tundra environments. ~~We compared~~ [Our results are essentially the same:](#) temporal and spatial coherence [between](#) in our [main](#) study area ~~and a, north of the tree line near CALM site U8 (almost entirely free of trees, (https://www2.gwu.edu/~calm/data/webforms/u8_f.html) are significantly better than those obtained in the~~ discontinuous permafrost region near Fairbanks, Alaska, ~~and obtained similar results. Decorrelation (section 5.5). Significant decorrelation also~~ occurred around CALM site U18 (~15 km southwest of Fairbanks, Alaska) during the 2023 thaw season. ~~)} Land cover here is open black spruce forest (https://www2.gwu.edu/~calm/data/webforms/u18_f.htm). In contrast, temporal and spatial coherence remained high at CALM site U8 site, located in the continuous permafrost region to the north. Land cover here is classified as graminoid-moss tundra and graminoid, prostrate-dwarf shrub and moss tundra (https://www2.gwu.edu/~calm/data/webforms/u8_f.html).~~ Longer wavelengths such as L-band may be more useful in densely vegetated terrains. The ~~launch of the NiSAR~~ [NISAR](#) mission, [scheduled for launch](#) in 2024, with its L-band wavelength and repeat frequency of 6-12 days, should prove useful for [more](#) densely vegetated ~~discontinuous~~ permafrost regions.

2. The spatial and temporal resolution of models that allow estimation of key ancillary parameters may limit accuracy in some regions, [especially for example](#) soil parameters from the GLDAS model, and

atmospheric parameters from ERA-5. The spatial resolution of GLDAS' soil parameter model is 0.25 degrees, an area that spans our study entire study area in the Alaska north slope. The temporal resolution of ERA-5 is adequate, but its spatial resolution precludes limits local analysis.

~~3. The model does not estimate long-term subsidence due to thawing of segregated ice, instead estimating ALT only by considering volume change from pore ice to water in the active layer. Development of a long-term (multi-year) ALT subsidence model is desirable.~~

~~4. Accurate and, dense and widespread porosity-depth profiles based on in-situ data would also improve ALT estimation: from remotely sensed data. In particular, empirical and statistical models of soil properties calibrated with in situ data could significantly improve radar-based ALT models (e.g., O'Connor et al., 2020; Bakian Dogaheh et al., 2020, 2022, 2023).~~ 

~~4. Variations in soil ice content and non-linear thaw season subsidence time series need to be considered (Zwieback et al., 2024).~~

~~6. Conclusions~~

We used Sentinel-1 interferometric SAR data in the from 2017 to 2022 around CALM site of northernU8 in Northern Alaska ~~for to measure~~ thaw season ~~2017 to 2022 to~~ subsidence and estimate active layer thickness ~~(with a widely used physical model that exploits the volume difference between ice and water. Limited ICESat-2 LiDAR data are consistent with InSAR estimates of seasonal subsidence. We do not attempt to estimate long term (multi-year) elevation change. Instead we estimate ALT) using interferometric analysis.~~ at the end of each thaw season and compare its yearly evolution, avoiding issues of decorrelation of the radar signal over the winter season.

ALT estimates in our study area range from ~20 cm to ~~larger~~ more than 150 cm ~~in our study area,~~ similar to in-situ measurements at the CALM site and previous remotely sensed estimates. Agreement with the later part of the quarter century-long CALM time series is notable and suggests that annual

ALT estimates from satellite InSAR can be effective at monitoring longer-term permafrost health, at least for Alaska's continuous permafrost zone north of the tree line. However, the technique was not effective in the discontinuous permafrost region of central Alaska near Fairbanks, reflecting decorrelation of the C-band radar signal, probably from heavy tree cover. At the northern study site, ALT shows high spatial and temporal variability in both the satellite and in-situ data sets, sometimes changing dramatically between adjoining adjacent 10 m cells. Subsidence rate also varies significantly between closely spaced points, ranging from ~3-20 cm/yr during the thaw season at our study locations. Applying atmospheric corrections to C-band radar images improves signal to noise ratio. Limited ICESat-2 LiDAR data is consistent with the InSAR estimates of seasonal subsidence. Our results suggest that InSAR could be used to assess long-term continuous permafrost changes in the region 2-18 mm/month at our northern study site during thaw season. The reasons for such high spatial and temporal variability of ALT are not clear and warrant further research.

Acknowledgments

This project was funded by grants to THD from the NASA Earth Science program (grant # 80NSS-C22K1106) and the Army Corps of Engineers (USACE Engineer Research and Development Center, Cooperative Agreement W9132V-22-2-0001). We thank Irena Hajnsek, Malte Vöge, Roger Michaelides, and Vincent Boulanger-Martel for detailed reviews that greatly improved the manuscript. We appreciate Regula Frauenfelder for editing the paper.

References

1. Bakian-Dogaheh, K., R.H. Chen, Y. Yi, T.D. Sullivan, R.J. Michaelides, A.D. Parsekian, K. Schaefer, A. Tabatabaeenejad, J. Kimball, and M. Moghaddam. 2023. Soil Matric Potential, Dielectric, and Physical Properties, Arctic Alaska, 2018. ORNL DAAC, Oak Ridge, Tennessee, USA. <https://doi.org/10.3334/ORNLDAAC/2149>
2. Bakian-Dogaheh, K., Chen, R. H., Yi, Y., Kimball, J. S., Moghaddam, M., and Tabatabaeenejad, A.: A model to characterize soil moisture and organic matter profiles in the permafrost active layer in support of radar remote sensing in Alaskan Arctic tundra, *Environmental Research Letters*, 17, 025 011, 2022.
3. Bakian-Dogaheh, K., R.H. Chen, M. Moghaddam, Y. Yi, and A. Tabatabaeenejad. 2020. ABoVE: Active Layer Soil Characterization of Permafrost Sites, Northern Alaska, 2018. ORNL DAAC, Oak Ridge, Tennessee, USA. <https://doi.org/10.3334/ORNLDAAC/1759>
4. Bekaert, D. P. S., Hamlington, B. D., Buzzanga, B., & Jones, C. E. (2017). Spaceborne synthetic aperture radar survey of subsidence in Hampton Roads, Virginia (USA). *Scientific reports*, 7(1), 14752.
25. Bernhard, P., Zwieback, S., Leinss, S., & Hajnsek, I. (2020). Mapping retrogressive thaw slumps using single-pass TanDEM-X observations. *IEEE Journal of Selected Topics in Applied Earth Observations and Remote Sensing*, 13, 3263-3280.
6. Bürgmann, R., Rosen, P. A., & Fielding, E. J. (2000). Synthetic aperture radar interferometry to measure Earth's surface topography and its deformation. *Annual review of earth and planetary sciences*, 28(1), 169-209.
37. Brown, J., Hinkel, K. M., & Nelson, F. E. (2000). The circumpolar active layer monitoring (CALM) program: research designs and initial results. *Polar geography*, 24(3), 166-258. <https://doi.org/10.1080/10889370009377698>

- | [48](#). Castellazzi, P., Martel, R., Galloway, D. L., Longuevergne, L., & Rivera, A. (2016). Assessing groundwater depletion and dynamics using GRACE and InSAR: Potential and limitations. *Groundwater*, 54(6), 768-780.
- | [59](#). Chen, C. W., & Zebker, H. A. (2002). Phase unwrapping for large SAR interferograms: Statistical segmentation and generalized network models. *IEEE Transactions on Geoscience and Remote Sensing*, 40(8), 1709-1719.
- | [610](#). Chen, J., Wu, Y., O'Connor, M., Cardenas, M. B., Schaefer, K., Michaelides, R., & Kling, G. (2020). Active layer freeze-thaw and water storage dynamics in permafrost environments inferred from InSAR. *Remote Sensing of Environment*, 248, 112007.
- | [711](#). Chen, R.H., R.J. Michaelides, J. Chen, A.C. Chen, L.K. Clayton, K. Bakian-Dogaheh, L. Huang, E. Jafarov, L. Liu, M. Moghaddam, A.D. Parsekian, T.D. Sullivan, A. Tabatabaenejad, E. Wig, H.A. Zebker, and Y. Zhao. (2022). ABoVE: Active Layer Thickness from Airborne L- and P- band SAR, Alaska, 2017, Ver. 3. ORNL DAAC, Oak Ridge, Tennessee, USA. <https://doi.org/10.3334/ORNLDAAC/2004>
- | [812](#). Chen, R. H., Michaelides, R. J., Zhao, Y., Huang, L., Wig, E., Sullivan, T. D., ... & Schaefer, K. M. (2023). Permafrost Dynamics Observatory (PDO): 2. Joint Retrieval of Permafrost Active Layer Thickness and Soil Moisture From L-Band InSAR and P-Band PolSAR. *Earth and Space Science*, 10(1), e2022EA002453.
- | [913](#). Clayton, L. K., Schaefer, K., Battaglia, M. J., Bourgeau-Chavez, L., Chen, J., Chen, R. H., ... & Zhao, Y. (2021). Active layer thickness as a function of soil water content. *Environmental Research Letters*, 16(5), 055028.
- | [1014](#). Dammann, D. O., Eriksson, L. E., Mahoney, A. R., Eicken, H., & Meyer, F. J. (2019). Mapping pan-Arctic landfast sea ice stability using Sentinel-1 interferometry. *The Cryosphere*, 13(2), 557-577.

- | ~~4115~~. Daout, S., Doin, M. P., Peltzer, G., Socquet, A., & Lasserre, C. (2017). Large-scale InSAR monitoring of permafrost freeze-thaw cycles on the Tibetan Plateau. *Geophysical Research Letters*, 44(2), 901-909.
- | ~~4216~~. Deng, F., T. H. Dixon, and S. Xie (2020) Surface deformation and induced seismicity due to fluid injection and oil and gas extraction in western Texas. *Journal of Geophysical Research: Solid Earth*, 125, <https://doi.org/10.1029/2019JB018962>.
- | ~~4317~~. Ding, X. L., Li, Z. W., Zhu, J. J., Feng, G. C., & Long, J. P. (2008). Atmospheric effects on InSAR measurements and their mitigation. *Sensors*, 8(9), 5426-5448.
- | ~~4418~~. Dobinski, W. (2011). Permafrost. *Earth-Science Reviews*, 108(3-4), 158-169.
- | ~~4519~~. Doin, M. P., Lasserre, C., Peltzer, G., Cavalié, O., & Doubre, C. (2009). Corrections of stratified tropospheric delays in SAR interferometry: Validation with global atmospheric models. *Journal of Applied Geophysics*, 69(1), 35-50.
- | *~~4620~~. European Space Agency, Sinergise (2021). Copernicus Global Digital Elevation Model. Distributed by OpenTopography. <https://doi.org/10.5069/G9028PQB>. Accessed: 2023-04-01
- | ~~4721~~. Fattahi, H., Agram, P., & Simons, M. (2016). A network-based enhanced spectral diversity approach for tops time-series analysis. *IEEE Transactions on Geoscience and Remote Sensing*, 55(2), 777–786.
- | ~~4822~~. Goldstein, R. M., & Werner, C. L. (1998). Radar interferogram filtering for geophysical applications. *Geophysical research letters*, 25(21), 4035-4038.
- | ~~4923~~. Grapenthin, R., Cheng, Y., Angarita, M., Tan, D., Meyer, F. J., Fee, D., & Wech, A. (2022). Return from Dormancy: Rapid inflation and seismic unrest driven by transcrustal magma transfer at Mt. Edgecumbe (L'úx Shaa) Volcano, Alaska. *Geophysical Research Letters*, 49(20), e2022GL099464.

- | [2024](#). Grigal, D. F., Brovold, S. L., Nord, W. S., & Ohmann, L. F. (1989). Bulk density of surface soils and peat in the north central United States. *Canadian Journal of Soil Science*, 69(4), 895-900.
- | [2125](#). Hanssen, R. F. (2001). *Radar interferometry: data interpretation and error analysis* (Vol. 2). Springer Science & Business Media.
- | [2226](#). Hersbach, H., Bell, B., Berrisford, P., Hirahara, S., Horányi, A., Muñoz-Sabater, J., ... & Thépaut, J. N. (2020). The ERA5 global reanalysis. *Quarterly Journal of the Royal Meteorological Society*, 146(730), 1999-2049.
- | [*2327](#). [Hinkel, K. M., & Nelson, F. E. \(2003\). Spatial and temporal patterns of active layer thickness at Circumpolar Active Layer Monitoring \(CALM\) sites in northern Alaska, 1995–2000. *Journal of Geophysical Research: Atmospheres*, 108\(D2\).](#)
- | [28](#). Hogenson, K., Kristenson, H., Kennedy, J., Johnston, A., Rine, J., Logan, T., Zhu, J., Williams, F., Herrmann, J., Smale, J., & Meyer, F. (2020). Hybrid Pluggable Processing Pipeline (HyP3): A cloud-native infrastructure for generic processing of SAR data [Computer software]. <https://doi.org/10.5281/zenodo.4646138>
- | [2429](#). Hossain, M. F., Chen, W., & Zhang, Y. (2015). Bulk density of mineral and organic soils in the Canada's arctic and sub-arctic. *Information processing in agriculture*, 2(3-4), 183-190.
- | [2530](#). Hu, Y., Liu, L., Larson, K. M., Schaefer, K. M., Zhang, J., & Yao, Y. (2018). GPS interferometric reflectometry reveals cyclic elevation changes in thaw and freezing seasons in a permafrost area (Barrow, Alaska). *Geophysical Research Letters*, 45(11), 5581-5589.
- | [2631](#). Iwahana, G., Uchida, M., Liu, L., Gong, W., Meyer, F. J., Guritz, R., ... & Hinzman, L. (2016). InSAR detection and field evidence for thermokarst after a tundra wildfire, using ALOS-PALSAR. *Remote Sensing*, 8(3), 218.

- | [2732](#). Jackson, R.B., H.A. Mooney, and E.-D. Schulze. 2003. Global Distribution of Fine Root Biomass in Terrestrial Ecosystems. ORNL DAAC, Oak Ridge, Tennessee, USA. <https://doi.org/10.3334/ORNLDAAC/658>
- | [2833](#). Johnson, K. D., Harden, J., McGuire, A. D., Bliss, N. B., Bockheim, J. G., Clark, M., ... & Valentine, D. W. (2011). Soil carbon distribution in Alaska in relation to soil-forming factors. *Geoderma*, 167, 71-84.
- | [2934](#). Jolivet, R., Grandin, R., Lasserre, C., Doin, M. P., & Peltzer, G. (2011). Systematic InSAR tropospheric phase delay corrections from global meteorological reanalysis data. *Geophysical Research Letters*, 38(17).
- | [3035](#). Jolivet, R., Agram, P. S., Lin, N. Y., Simons, M., Doin, M. P., Peltzer, G., & Li, Z. (2014). Improving InSAR geodesy using global atmospheric models. *Journal of Geophysical Research: Solid Earth*, 119(3), 2324-2341.
- | [3136](#). Liu, L., Jafarov, E. E., Schaefer, K. M., Jones, B. M., Zebker, H. A., Williams, C. A., ... & Zhang, T. (2014). InSAR detects increase in surface subsidence caused by an Arctic tundra fire. *Geophysical Research Letters*, 41(11), 3906-3913.
- | [3237](#). Liu, L., Schaefer, K. M., Chen, A. C., Gusmeroli, A., Zebker, H. A., & Zhang, T. (2015). Remote sensing measurements of thermokarst subsidence using InSAR. *Journal of Geophysical Research: Earth Surface*, 120(9), 1935-1948.
- | [3338](#). Liu, L., Schaefer, K., Zhang, T., & Wahr, J. (2012). Estimating 1992–2000 average active layer thickness on the Alaskan North Slope from remotely sensed surface subsidence. *Journal of Geophysical Research: Earth Surface*, 117(F1).
- | [3439](#). Liu, L., Zhang, T., & Wahr, J. (2010). InSAR measurements of surface deformation over permafrost on the North Slope of Alaska. *Journal of Geophysical Research: Earth Surface*, 115(F3).

[3540. Martino, A. J., Neumann, T. A., Kurtz, N. T., & McLennan, D. \(2019, October\). ICESat-2 mission overview and early performance. In *Sensors, systems, and next-generation satellites XXIII* \(Vol. 11151, pp. 68-77\). SPIE. <https://doi.org/10.1117/12.2534938>](#)

[41. Meyer, F., Kampes, B., Bamler, R., & Fischer, J. \(2006, February\). Methods for atmospheric correction in InSAR data. In *Fringe 2005 Workshop* \(Vol. 610\).](#)

[3642. Meyer, F. J. \(2011\). Performance requirements for ionospheric correction of low-frequency SAR data. *IEEE transactions on geoscience and remote sensing*, 49\(10\), 3694-3702.](#)

[3743. Michaelides, R. J., Bryant, M. B., Siegfried, M. R., & Borsa, A. A. \(2021\). Quantifying Surface-Height Change Over a Periglacial Environment With ICESat-2 Laser Altimetry. *Earth and Space Science*, 8\(8\), e2020EA001538.](#)

[44. Mishra, U., & Riley, W. J. \(2012\). Alaskan soil carbon stocks: spatial variability and dependence on environmental factors. *Biogeosciences*, 9\(9\), 3637-3645.](#)

[3845. Nelson, F. E., Shiklomanov, N. I., Mueller, G. R., Hinkel, K. M., Walker, D. A., & Bockheim, J. G. \(1997\). Estimating active-layer thickness over a large region: Kuparuk River basin, Alaska, USA. *Arctic and Alpine Research*, 29\(4\), 367-378.](#)

[46. Nelson, F. E., Shiklomanov, N. I., & Mueller, G. R. \(1999\). Variability of active-layer thickness at multiple spatial scales, north-central Alaska, USA. *Arctic, Antarctic, and Alpine Research*, 31\(2\), 179-186.](#)

[47. Nelson, F. E., Hinkel, K. M., Shiklomanov, N. I., Mueller, G. R., Miller, L. L., & Walker, D. A. \(1998\). Active-layer thickness in north central Alaska: Systematic sampling, scale, and spatial autocorrelation. *Journal of Geophysical Research: Atmospheres*, 103\(D22\), 28963-28973.](#)

[48. Neuenschwander, A. L., & Magruder, L. A. \(2019\). Canopy and terrain height retrievals with ICESat-2: A first look. *Remote sensing*, 11\(14\), 1721.](#)

4049. Neuenschwander, A., & Pitts, K. (2019). The ATL08 land and vegetation product for the ICESat-2 Mission. *Remote sensing of environment*, 221, 247-259.

4150. Neuenschwander, A., Pitts, K., Jelley, B., Robbins, J., Markel, J., Popescu, S., ... & Klotz, B. (2019). Ice, Cloud, and Land Elevation Satellite 2 (ICESat-2) algorithm theoretical basis document (ATBD) for land-vegetation along-track products (ATL08). *National Aeronautics and Space Administration: Washington, DC, USA*.

51. Neuenschwander, A. L., K. L. Pitts, B. P. Jelley, J. Robbins, B. Klotz, S. C. Popescu, R. F. Nelson, D. Harding, D. Pederson, and R. Sheridan. (2021). ATLAS/ICESat-2 L3A Land and Vegetation Height, Version 5. [Indicate subset used]. Boulder, Colorado USA. NASA National Snow and Ice Data Center Distributed Active Archive Center. <https://doi.org/10.5067/ATLAS/ATL08.005>.

4252. O'Connor, M. T., Cardenas, M. B., Ferencz, S. B., Wu, Y., Neilson, B. T., Chen, J., & Kling, G. W. (2020). Empirical models for predicting water and heat flow properties of permafrost soils. *Geophysical Research Letters*, 47(11), e2020GL087646.

53. Peddle, D. R., & Franklin, S. E. (1993). Classification of permafrost active layer depth from remotely sensed and topographic evidence. *Remote Sensing of Environment*, 44(1), 67-80.

4354. Ping, C. L., J. D. Jastrow, M. T. Jorgenson, G. J. Michaelson, and Y. L. Shur (2015) Permafrost soils and carbon cycling. *Soil*, 1, 147–171, doi:10.5194/soil-1-147-2015

55. Poland, M. P., & Zebker, H. A. (2022). Volcano geodesy using InSAR in 2020: the past and next decades. *Bulletin of Volcanology*, 4(3), 27.

4456. Price, J. S., Cagampan, J., & Kellner, E. (2005). Assessment of peat compressibility: is there an easy way?. *Hydrological Processes: An International Journal*, 19(17), 3469-3475.

4557. Riseborough, D. W. (2003). Thawing and freezing indices in the active layer. In Proceedings of the 8th International Conference on Permafrost (Vol. 2, pp. 953-958). Rotterdam: AA Balkema.

- | [4658](#). Rodell, M., P.R. Houser, U. Jambor, J. Gottschalck, K. Mitchell, C.-J. Meng, K. Arsenault, B. Cosgrove, J. Radakovich, M. Bosilovich, J.K. Entin, J.P. Walker, D. Lohmann, and D. Toll, The Global Land Data Assimilation System, *Bull. Amer. Meteor. Soc.*, 85(3), 381-394, 2004.
- | [4759](#). Rosen, P. A., Gurrola, E., Sacco, G. F., & Zebker, H. (2012). The InSAR scientific computing environment. In *Eusar 2012; 9th European conference on synthetic aperture radar* (pp. 730–733).
- | [4860](#). Rykhus, R. P., & Lu, Z. (2008). InSAR detects possible thaw settlement in the Alaskan Arctic Coastal Plain. *Canadian Journal of Remote Sensing*, 34(2), 100-112.
- | [4961](#). Sadeghi Chorsi, T., Braunmiller, J., Deng, F., Mueller, N., Kerstetter, S., Stern, R. J., & Dixon, T. H. (2022). The May 15, 2020 M 6.5 Monte Cristo Range, Nevada, earthquake: eyes in the sky, boots on the ground, and a chance for students to learn. *International Geology Review*, 64(19), 2683-2702.
- | [5062](#). Sadeghi Chorsi, T., Braunmiller, J., Deng, F., & Dixon, T. H. (2022). Afterslip From the 2020 M 6.5 Monte Cristo Range, Nevada Earthquake. *Geophysical Research Letters*, 49(17), e2022GL099952.
- | [5163](#). Schaefer, K., Zhang, T., Slater, A. G., Lu, L., Etringer, A., & Baker, I. (2009). Improving simulated soil temperatures and soil freeze/thaw at high-latitude regions in the Simple Biosphere/Carnegie-Ames-Stanford Approach model. *Journal of Geophysical Research: Earth Surface*, 114(F2).
- | [5264](#). Schaefer, K., Liu, L., Parsekian, A., Jafarov, E., Chen, A., Zhang, T., ... & Schaefer, T. (2015). Remotely sensed active layer thickness (ReSALT) at Barrow, Alaska using interferometric synthetic aperture radar. *Remote sensing*, 7(4), 3735-3759.
- | [5365](#). [Smith, B., Fricker, H. A., Holschuh, N., Gardner, A. S., Adusumilli, S., Brunt, K. M., ... & Siegfried, M. R. \(2019\). Land ice height-retrieval algorithm for NASA's ICESat-2 photon-counting laser altimeter. *Remote Sensing of Environment*, 233, 111352.](#)

66. [Strozzi, T., Caduff, R., Jones, N., Barboux, C., Delaloye, R., Bodin, X., ... & Schrott, L. \(2020\). Monitoring rock glacier kinematics with satellite synthetic aperture radar. *Remote Sensing*, 12\(3\), 559.](#)

67. [US Department of Agriculture \(1999\) Soil Taxonomy: A Basic System of Soil Classification for Making and Interpreting Soil Surveys, 2nd Edn., Agric. Handb. 436, USDA-NRCS, US Gov. Print. Office, Washington, DC.](#)

68. Vasco, D. W., T. H. Dixon, A. Ferretti, S.V. Samsonov (2020) Monitoring the fate of injected CO₂ using geodetic techniques, *The Leading Edge*, 39 (1), 29-37.

5469. Wang, L., Marzahn, P., Bernier, M., & Ludwig, R. (2020). Sentinel-1 InSAR measurements of deformation over discontinuous permafrost terrain, Northern Quebec, Canada. *Remote Sensing of Environment*, 248, 111965.

5570. Yang, Q., W. Zhao, T. H. Dixon, F. Amelung, W. S. Han, P. Li (2015) InSAR monitoring of ground deformation due to CO₂ injection at an Enhanced Oil Recovery Site, West Texas. *International Journal of Greenhouse Gas Control* 41, 116-126, doi:10.1016/j.ijggc.2015.06.016

5671. Zhang, X., Jones, C. E., Oliver-Cabrera, T., Simard, M., & Fagherazzi, S. (2022). Using rapid repeat SAR interferometry to improve hydrodynamic models of flood propagation in coastal wetlands. *Advances in Water Resources*, 159, 104088.

*5772. [Zwieback, S., Kokelj, S. V., Günther, F., Boike, J., Grosse, G., & Hajsek, I. \(2018\). Sub-seasonal thaw slump mass wasting is not consistently energy limited at the landscape scale. *The Cryosphere*, 12\(2\), 549-564.](#)

73. (<https://www.ncei.noaa.gov/maps/daily/>)

~~Clayton, L. K., Schaefer, K., Battaglia, M. J., Bourgeau-Chavez, 74. Zwieback, S., Iwahana, G., Sakhalkar, S., Biessel, R., Taylor, S., & Meyer, F. J. (2024). Excess ground ice profiles in continuous permafrost mapped from InSAR subsidence. *Water Resources Research*, 60(2), e2023WR035331.~~

~~L., Chen, J., Chen, R. H., ... & Zhao, Y. (2021). Active layer thickness as a function of soil water content. *Environmental Research Letters*, 16(5), 055028.~~